

High-Contrast Electrooptic Modulation of a Photonic Crystal Nanocavity by Electrical Gating of Graphene

Xuetao Gan,[†] Ren-Jye Shiue,[†] Yuanda Gao,[‡] Kin Fai Mak,[⊥] Xinwen Yao,[†] Luozhou Li,[†] Attila Szep,[§] Dennis Walker, Jr.,[§] James Hone,[‡] Tony F. Heinz,^{†,⊥} and Dirk Englund^{*,†,||}

[†]Department of Electrical Engineering, Columbia University, New York, New York 10027, United States

[‡]Department of Mechanical Engineering, Columbia University, New York, New York 10027, United States

[⊥]Department of Physics, Columbia University, New York, New York 10027, United States

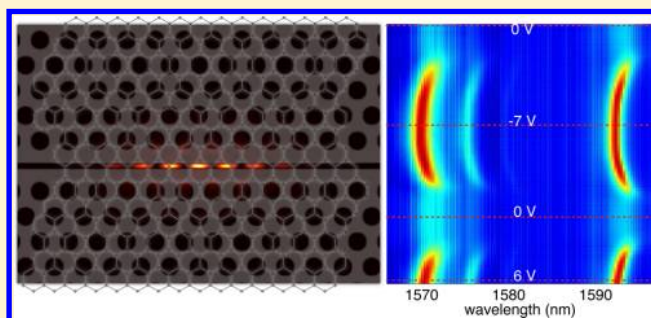
[§]Air Force Research Laboratory, Sensors Directorate, WPAFB, Dayton, Ohio 45433, United States

^{||}Department of Applied Physics and Applied Mathematics, Columbia University, New York, New York 10027, United States

Supporting Information

ABSTRACT: We demonstrate high-contrast electro-optic modulation of a photonic crystal nanocavity integrated with an electrically gated monolayer graphene. A silicon air-slot nanocavity provides strong overlap between the resonant optical field and graphene. Tuning the Fermi energy of the graphene layer to 0.85 eV enables strong control of its optical conductivity at telecom wavelengths, which allows modulation of cavity reflection in excess of 10 dB for a swing voltage of only 1.5 V. The cavity resonance at 1570 nm is found to undergo a shift in wavelength of nearly 2 nm, together with a 3-fold increase in quality factor. These observations enable a cavity-enhanced determination of graphene's complex optical sheet conductivity at different doping levels. Our simple device demonstrates the feasibility of high-contrast, low-power, and frequency-selective electro-optic modulators in graphene-integrated silicon photonic integrated circuits.

KEYWORDS: Graphene, optoelectronics, electro-optic modulation, photonic crystal cavity



Graphene's unusual optical properties enable a range of promising optoelectronic applications.^{1–6} To enhance the light-matter interaction in this single atomic layer material, graphene has been integrated into optical waveguides and cavities, and has as well been used to support surface plasmon polariton states.^{5,7–16} In the limit of wavelength-scale confinement, we recently demonstrated a dramatic enhancement of the light-matter interaction in graphene coupled to a planar photonic crystal (PPC) nanocavity, leading to a reduction in the cavity reflectivity by more than 20 dB.¹⁷ Here, we demonstrate high contrast electro-optic modulation of the reflectivity of a PPC nanocavity by electrical gating of the graphene layer. Relying on the high Fermi velocity and monolayer thickness of graphene, we tune its Fermi energy to as much as 0.85 eV. We thereby obtain a cavity modulation in excess of 10 dB, which, while limited in speed for our current method of electrochemical gating, clearly shows the capability for strong modulation of light in this very compact device geometry. Furthermore, we employ efficient coupling between the cavity modes and graphene for precision spectroscopy of graphene in the near-infrared spectral range as a function of doping level. Our measurements yield a complex optical sheet conductivity of monolayer graphene that agrees well with a theoretical model of the material's optical sheet conductivity.

As shown schematically in Figure 1a, the experimental device consists of an air-suspended PPC nanocavity that is coupled to a graphene field-effect transistor (FET) gated by a solid electrolyte.^{18,19} The optical transmission of monolayer graphene for an incident photon at frequency ω is modulated by electrostatically tuning the graphene's Fermi energy (E_F). As indicated in Figure 1b, when E_F is tuned away from the Dirac point by more than half of the photon energy $\hbar\omega/2$, the interband transitions are Pauli blocked, reducing the graphene absorption.^{20,21} Thus, the reflectivity and Q factor of the cavity can be controlled by modulating the doping level of graphene.¹⁷

To improve the overlap between graphene and cavity resonance modes, we employ an air-slot PPC nanocavity²² with strongly confined modes in a central air-gap, as shown in Figure 1c. This design increases the coupling strength of the optical mode to the graphene sheet by almost a factor of 3 compared to the linear three-hole defect cavity used previously,¹⁷ where light is confined in the high index material²³ and experiences less overlap with the graphene layer. The air-

Received: November 26, 2012

Revised: January 11, 2013

Published: January 17, 2013

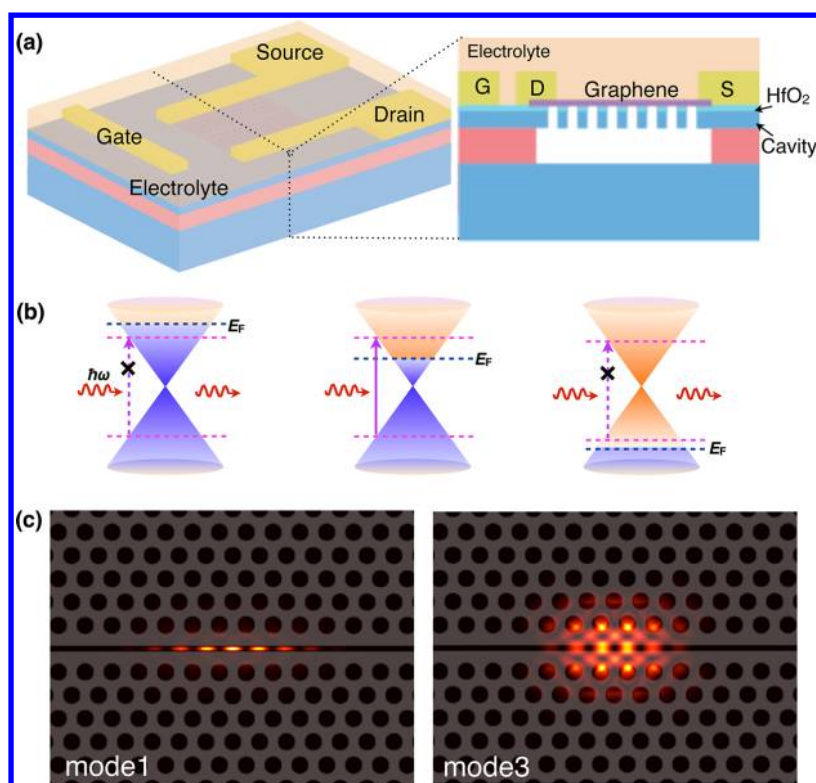


Figure 1. (a) Schematic of the electrically controlled graphene-PPC nanocavity. The reflection of the air-suspended cavity can be modulated by electrostatic tuning of the Fermi level of graphene layer using electrolyte gating. A thin HfO_2 layer is grown on PPCs before the graphene transfer to isolate the silicon PPCs and graphene electrically. (b) Band structure of graphene at different doping levels; graphene becomes more transparent when interband transitions are Pauli blocked, as shown in images on the left and right. (c) Simulated energy distributions of two resonant modes of the air-slot cavity (left, mode1; right, mode3 as defined in Figure 2c) based on a finite-difference time-domain (FDTD) technique. The optical field is confined in the air-gap, enabling a strong coupling with graphene.

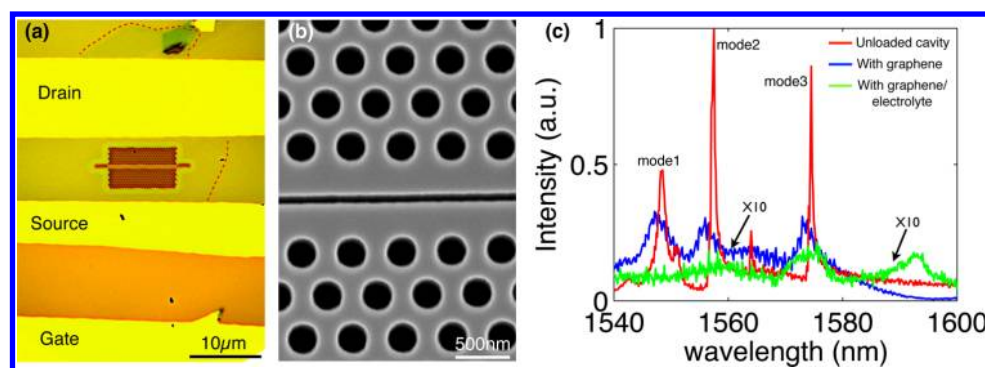


Figure 2. (a) Optical image of one of the electrically controlled graphene-PPC nanocavity devices. The graphene monolayer covers an air-slot cavity; the boundary of the graphene is indicated by the red dashed line. Source and drain electrodes are near the cavity, while the gate electrode is removed by $15\ \mu\text{m}$. (b) SEM image of the air-slot cavity before graphene deposition; AFM and SEM studies of PPC cavities after graphene deposition are shown in previous work.¹⁷ The lattice spacing is $a = 450\ \text{nm}$, and the hole radius is $r = 150\ \text{nm}$. The defect of the cavity is formed by a slight outward shift of the central three rows of holes on both sides of the slot. (c) Reflection spectra of the PPC cavity covered with HfO_2 layer, after graphene transfer (blue), and after deposition of the electrolyte (green), showing three dominant resonant modes (modes 1, 2, and 3). The cavity resonances present clear drops of the reflected intensities and Q factors after the graphene transfer.

slot PPC nanocavities are fabricated on a silicon-on-insulator wafer with a 220 nm-thick silicon membrane using a combination of electron-beam lithography and dry/wet etching steps. We employ mechanically exfoliated graphene monolayers, which are transferred onto the PPC nanocavities using a precision alignment technique.²⁴ The drain, source, and gate electrodes of the graphene FET are fabricated using electron-beam lithography and titanium/gold electron-beam evaporation. In early trials, we found that these contacts can gate the

intrinsic or lightly doped silicon membrane directly and influence the cavity spectroscopy under electrical gating. To avoid this effect, the devices described in this study include a conformal 10 nm hafnium oxide (HfO_2) layer grown on the PPCs using an atomic layer deposition before the graphene transfer (see Figure 1a).

Figure 2a displays an optical image of one of the completed graphene-PPC nanocavity devices. The dashed red line traces the boundary of the monolayer graphene, as confirmed using

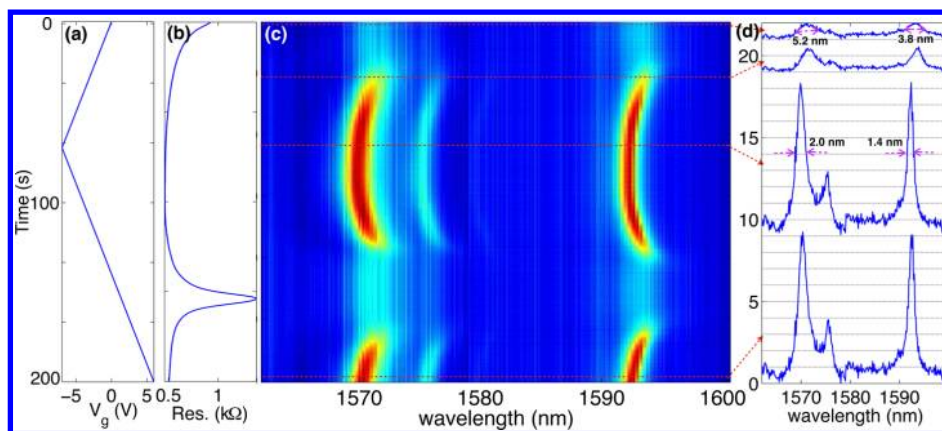


Figure 3. Electrical and optical responses of the electrically controlled graphene-PPC nanocavity. (a) Gate voltage V_g modulated in a sawtooth pattern at a rate of 0.1 V/s between -7 and 6 V. (b) DC resistance across the graphene layer measured from the source to drain electrodes, showing the charge neutrality point at $V_{CN} = 1$ V. (c) Reflection spectra of the cavity as V_g is modulated. The resonances show clear shifts in wavelength and modulations of Q factors and intensities under different gate-voltages. (d) Spectra of the cavity reflection for $V_g = 0, -1, -7$, and 6 V, which are normalized by the reflection peak at $V_g = 0$. Compared to the reflection of the graphene-PPC nanocavity at zero-bias, the cavity presents ~ 8.5 times higher peaks when the single-layer graphene is strongly doped. For a voltage swing from -1 to -2.5 V, we observe a modulation of the cavity reflection by more than 10 dB at a wavelength of 1592.9 nm.

micro-Raman spectroscopy. The gate electrode is located about $15 \mu\text{m}$ away from the graphene flake to ensure effective doping through the electrolyte. Figure 2b displays a scanning electron microscope (SEM) image of the air-slot cavity with a lattice spacing of $a = 450$ nm and a lattice hole radius of $r = 150$ nm. The cavity defect is formed by shifting air-holes away from the central slot.²² After graphene is transferred and the metal contacts are prepared, an electrolyte (PEO plus LiClO_4) layer is spin-coated on the entire wafer, providing high electrical fields and carrier densities in graphene.^{18,19}

We characterize the graphene-PPC nanocavity using a cross-polarization confocal microscope with a broad-band (super-continuum laser) excitation source.^{17,25} The cavity reflection is analyzed using a spectrometer with a resolution of 0.05 nm. This vertical coupling to the cavity has relatively low efficiency, which results in a large insertion loss for the device. With further development of this technology, efficient coupling strategies, such as the use of tapered fibers²⁶ or on-chip waveguide couplers,²⁷ could be employed to reduce the insertion loss.

The red curve in Figure 2c displays the reflection spectrum of the cavity before the graphene transfer and after the HfO_2 deposition, showing three dominant resonant modes²² at wavelengths of $\lambda_1 = 1548.4$ nm (mode1), $\lambda_2 = 1557.4$ nm (mode2), and $\lambda_3 = 1574.5$ nm (mode3). Fitting these resonances to Lorentzian curves, we estimate Q factors of $Q_i = 860, 2350, 3420$ for modes $i = 1, 2, 3$. These values are lower than the theoretically predicted Q factors obtained by the FDTD simulations, which are 12000, 16600, and 40400 for modes $i = 1, 2, 3$. We attribute the degradation of Q factors to fabrication tolerances. After the graphene transfer process, we observe blue-shifts of the three resonant wavelengths by 0.6, 1.0, and 0.9 nm, respectively; this is expected as a result of the decrease in the refractive index of the HfO_2 layer during the thermal annealing step of the graphene transfer process (see Supporting Information).²⁴ The single-layer graphene causes a strong reduction (nearly 18 dB) in the reflectivities of each of the three resonant modes, while their Q factors drop to 350, 640, and 440, respectively. Employing perturbation theory to the graphene-PPC cavity system,¹⁷ we calculate that the energy

decay rates induced by the graphene absorption are $\kappa_{\text{gr}} = (1.6, 1.1, 2.0) \times 10^{-3} \omega_i$ for these three resonant modes, where $\omega_i = 2\pi c/\lambda_i$ are the frequencies of the resonances. The variation in these loss rates is due to the different coupling rates between the graphene sheet and the electrical field distributions of the resonant modes: modes 1 and 3 have stronger optical fields—and therefore greater overlap with graphene—in the air-gap than mode 2.

The electrolyte deposition subsequently red-shifts the cavity resonances due to its real dielectric constant of about 2.5,²⁸ as shown in the green curve of Figure 2c. We also observe the broadening of the resonant peaks due to an extra optical loss from the electrolyte, which reduces the Q factors to $Q_{1,2,3} = 335, 610, 410$. This electrolyte-related loss amounts to extra $\kappa_{\text{electro}} = (1.3, 0.8, 1.7) \times 10^{-4} \omega_i$ for the three modes, respectively. As seen in Figure 2c, modes 1 and 2 become indistinguishable after electrolyte deposition because they experience varying red-shifts due to different mode-overlaps with the electrolyte (see Supporting Information).

To study the electrical control of the graphene-PPC nanocavity, we measure the cavity reflectivity as a function of the gate voltage V_g between the gate and drain electrodes. The sample is loaded in a vacuum chamber evacuated to pressures of 10^{-4} Torr at room temperature to avoid degradation of the electrolyte. The electrical resistance through the drain and source is monitored simultaneously to record the doping level of graphene. Figure 3 presents measurements of the electrical and optical signals of the graphene-PPC nanocavity as the gate voltage V_g is swept linearly. Here we scan V_g in a sawtooth pattern at a speed of 0.1 V/s between -7 and 6 V. The resistance peak across the graphene FET shown in Figure 3b indicates a gate voltage for the charge neutrality point of $V_{CN} = 1$ V. In Figure 3c, we present the cavity reflection spectra, acquired continuously at 30 frames per second during the voltage sweep. We first apply the bias along the negative direction. For small V_g ($-1 \text{ V} \leq V_g \leq 0 \text{ V}$), the cavity reflection remains unchanged, showing two resonant peaks at wavelengths of 1571.7 and 1593 nm for modes 1 and 3, respectively (top panel of Figure 3d). As V_g is decreased to -1 V, the two resonant peaks narrow (Q increases) and red shift slightly

(second panel of Figure 3d). This increase of the cavity reflectivity and Q factor arises from decreased cavity loss as the graphene absorption is reduced by Pauli blocking. Decreasing V_g further, we find that the resonant peaks continue to grow and narrow sharply over a voltage range of ~ 1.5 V, while the resonant wavelengths now blue-shift. The Q factor and reflectivity stabilize as V_g drops below -2.5 V, where the graphene achieves full Pauli blocking for the resonant modes. At $V_g = -7$ V, the peaks become very narrow and modes 1 and 2 again become distinguishable (third panel of Figure 3d). We observe the corresponding changes in Q factor when increasing V_g from -7 V back to 0 V. The behavior for positive bias voltage (with electron, rather than hole doping of graphene) mirrors that for negative voltages, taking into account the offset from the point of charge neutrality of $V_g = -1$ V. In terms of the overall response to gating, we see that the height of the resonance peaks increases by a factor of 8.5 for highly (electron or hole) doped graphene compared to the case of lightly doped graphene. Since the peaks also shift in wavelength with doping, the modulation at the peak wavelength for the highly doped graphene is still greater. For example, at a wavelength of 1592.9 nm, we obtain a modulation depth exceeding 10 dB for a swing in gate voltage between -1 V and -2.5 V. Over this voltage range, the Fermi energy shifts past $E_F = \hbar\omega/2$ for the onset of Pauli blocking. The need for a voltage swing as large as 1.5 V reflects broadening of the optical response in the vicinity of Pauli blocking. We expect that this could be decreased by reducing charge inhomogeneity and disorder effects,^{21,29} leading to a still lower modulation voltage.

Fitting the response of modes 1 and 3 to a Lorentzian form, we obtain Q factors and resonant wavelength shifts as a function of V_g from -6 to 6 V (Figure 4a,b). The gate-voltage

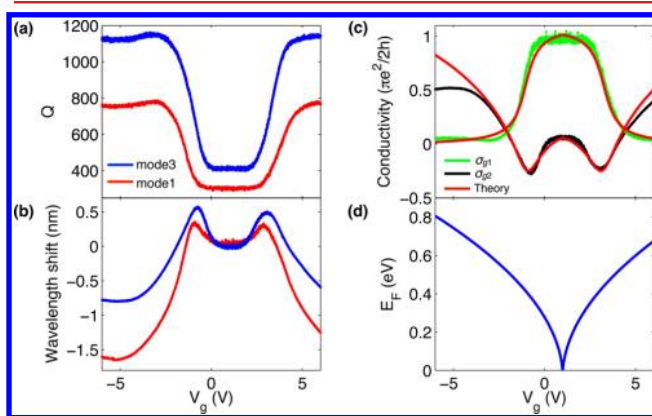


Figure 4. (a) Measured variations of the Q factors and (b) wavelength shifts for modes 1 and 3 as a function of V_g . (c) Complex optical sheet conductivity of graphene as a function of V_g as deduced from the experimental data of mode 3 in parts a and b. The red curves are the theoretical values determined by a model with interband and intraband transitions. (d) Fermi energy E_F of graphene calculated from the measured resistance between the drain and source electrodes under different gate voltage V_g .

at which the Q factor grows is greater for mode 1 than for mode 3, as expected from the slightly higher threshold for Pauli blocking of higher energy mode 1. For large V_g , the Q factor of both modes saturate, growing from 335 (410) to 740 (1150) for mode 1 (3). The recovered Q factors are lower than those before the graphene transfer (Q factors indicated in the red curve of Figure 2c). Considering the photon loss caused by the

electrolyte ($\kappa_{\text{electro},1,3} = (1.3, 1.7) \times 10^{-4} \omega_i$), we expect that modes 1 and 3 should have Q factors of 775 and 2160 in the limit of full transparency of graphene. The incomplete recovery of the Q factors indicates the presence of a small residual absorption in graphene even when the doping level is far above the threshold for Pauli blocking.²¹ The unrecovered Q factors caused by the electrolyte and residual absorption on graphene result in an insertion loss of the modulator, which is given by $10 \log_{10}(R_i/R_0)$, where R_i and R_0 are the reflections of the cavity with and without the residual loss. From coupled mode theory,¹⁷ the insertion loss can be calculated from $10 \log_{10}(Q_i/Q_0)^2$, where Q_i and Q_0 are the quality factors of the cavity with and without the residual loss. Using the experimental values for the Q factors, we then obtain losses of 1.3 and 9.4 dB, for modes 1 and 3, respectively, which are comparable to those achieved for other electro-optic modulators.³⁰ Figure 4b depicts the variation in the wavelengths of cavity resonances with gating; total excursions of 2 and 1.3 nm are found for modes 1 and 3, respectively.

The observed variation of the Q factors and wavelengths of the resonances arises from the variation in the complex in-plane optical sheet conductivity $\sigma_g = \sigma_{g1} + i\sigma_{g2}$ of graphene induced by doping.¹⁷ We can calculate σ_g from a knowledge of the overlap of the cavity modes (shown in Figure 1c) with the graphene layer using perturbation theory.¹⁷ The inferred values of σ_g from mode 3 are shown in Figure 4c. To understand the experimental data, we also plot (Figure 4d) the Fermi energy of the graphene sheet as a function of V_g from the capacitance of the polymer electrolyte ($\sim 1 \mu\text{Fcm}^{-2}$).¹⁸ After accounting for the photon loss caused by the electrolyte, we obtain a value of $\sigma_{g1} \approx \pi e^2/2h$ at V_{CN} , which decreases to a minimum value of $0.06(\pi e^2/(2h))$ at $V_g - V_{CN} = 3$ V. The value does not change appreciably for higher $V_g - V_{CN}$, with graphene displaying a finite absorption even for E_F significantly greater than $\hbar\omega/2$. This finite residual absorption (nonzero σ_{g1}) of graphene has been previously reported^{21,29} and has been attributed to the presence of midgap states and of electron–phonon coupling.³¹ On the other hand, σ_{g2} decreases monotonically from nearly zero at the charge neutrality point to a minimum of $-0.28(\pi e^2/(2h))$ at $V_g - V_{CN} = 1.8$ V. It then increases monotonically with increasing doping level. The inflection point for the variation of the imaginary part of the conductivity with doping is expected to occur at $E_F = \hbar\omega/2$.³² For our resonance at 1590 nm, we then predict the inflection point at $E_F = 0.39$ eV, which agrees well with the experimental data in Figure 4.

More generally, we can compare the experimentally deduced variation of the complex conductivity of graphene as a function of doping with a simple theoretical model based on both inter- and intraband transitions:^{32,33}

$$\sigma_g = \sigma_0 \Theta(\hbar\omega - 2E_F) + i\sigma_0 [(4E_F)/(\pi\hbar\omega) - 1/\pi \ln | (2E_F + \hbar\omega)/(2E_F - \hbar\omega) |] \quad (1)$$

with $\sigma_0 = e^2/(4\hbar)$. This model neglects finite temperature and finite dephasing rates. To take these effects into account, as well as possible inhomogeneity in the doping density, we broaden the predicted material response by convoluting formula 1 with a Lorentzian with a width of 50 meV. The corresponding theoretical prediction generally matches both the real and imaginary parts of the measured complex conductivity as a function of doping quite well (Figure 4c).

In conclusion, we have demonstrated that coupling an electrically gated graphene monolayer to a PPC nanocavity

allows the realization of strong optical modulation. While the speed of the current device is limited by the ionic mobility of the solid electrolyte,³⁴ the use of highly doped silicon PPC cavity as a back gate or the inclusion of dual-gated graphene layers should permit an increase of the modulation speed into the GHz regime.^{5,35} Because of the small capacitance of such graphene–PPC devices, we also anticipate low power consumption. For the current device, we estimate a switching energy of about 340 fJ from a calculation of the capacitive charging energy (see Supporting Information).³⁶ By reducing the lateral extent of the graphene sheet to cover only the defect region of the nanocavity, which is smaller than $0.5\ \mu\text{m}^2$ in area, we estimate that this energy consumption can be reduced below 1 fJ per bit, lower than that of current state-of-the-art resonator-based electro-optic modulators.^{36,37} Moreover, the PPC-based modulator is relatively broad-band, over 300 GHz for a Q value of 600, which promises greater temperature tolerance than for high-Q resonators. The potential for low power consumption, relatively wide bandwidth, and high modulation depth promise a new generation of high-performance graphene-based nanocavity modulators in photonic integrated circuits.

■ ASSOCIATED CONTENT

Supporting Information

Characterization of a compared cavity and energy consumption of the electrically controlled graphene–PPC nanocavity. This material is available free of charge via the Internet at <http://pubs.acs.org/>.

■ AUTHOR INFORMATION

Corresponding Author

*E-mail: englund@columbia.edu.

Notes

The authors declare no competing financial interest.

■ ACKNOWLEDGMENTS

Financial support was provided by the Air Force Office of Scientific Research PECASE, supervised by Dr. Gernot Pomrenke. Additional support was provided by the National Science Foundation through Grant DMR-1106225. Fabrication of the PPC was carried out at the Center for Functional Nanomaterials, Brookhaven National Laboratory, which is supported by the U.S. Department of Energy, Office of Basic Energy Sciences, under Contract No. DE-AC02-98CH10886. Device assembly, including graphene transfer, and characterization was supported by the Center for Re-Defining Photovoltaic Efficiency Through Molecule Scale Control, an Energy Frontier Research Center funded by the U.S. Department of Energy, Office of Science, Office of Basic Energy Sciences under Award Number DE-SC0001085.

■ REFERENCES

- (1) Bonaccorso, F.; Sun, Z.; Hasan, T.; Ferrari, A. C. *Nat. Photonics* **2010**, *4*, 611–622.
- (2) Konstantatos, G.; Badioli, M.; Gaudreau, L.; Osmond, J.; Bernechea, M.; de Arquer, F. P. G.; Gatti, F.; Koppens, F. H. L. *Nature Nanotechnol.* **2012**, *7*, 363–368.
- (3) Xia, F.; Mueller, T.; Lin, Y.-M.; Valdes-Garcia, A.; Avouris, P. *Nature Nanotechnol.* **2009**, *4*, 839–843.
- (4) Lemme, M. C.; Koppens, F. H. L.; Falk, A. L.; Rudner, M. S.; Park, H.; Levitov, L. S.; Marcus, C. M. *Nano Lett.* **2011**, *11*, 4134–7.
- (5) Liu, M.; Yin, X.; Ulin-Avila, E.; Geng, B.; Zentgraf, T.; Ju, L.; Wang, F.; Zhang, X. *Nature* **2011**, *474*, 64–7.
- (6) Sun, Z.; Hasan, T.; Torrisi, F.; Popa, D.; Privitera, G.; Wang, F.; Bonaccorso, F.; Basko, D. M.; Ferrari, A. C. *ACS Nano* **2010**, *4*, 803–810.
- (7) Furchi, M.; Urich, A.; Pospischil, A.; Lilley, G.; Unterrainer, K.; Detz, H.; Klang, P.; Andrews, A. M.; Schrenk, W.; Strasser, G.; Mueller, T. *Nano Lett.* **2012**, *12*, 2773–7.
- (8) Engel, M.; Steiner, M.; Lombardo, A.; Ferrari, A. C.; Löhneysen, H. V.; Avouris, P.; Krupke, R. *Nature Commun.* **2012**, *3*, 906.
- (9) Gu, T.; Petrone, N.; Mcmillan, J. F.; Zande, A. V. D.; Yu, M.; Lo, G. Q.; Kwong, D. L.; Hone, J.; Wong, C. W. *Nature Photonics* **2012**, *43*, 1–6.
- (10) Ju, L.; Geng, B.; Horng, J.; Girit, C.; Martin, M.; Hao, Z.; Bechtel, H. A.; Liang, X.; Zettl, A.; Shen, Y. R.; Wang, F. *Nature Nanotechnol.* **2011**, *6*, 630–4.
- (11) Koppens, F. H. L.; Chang, D. E.; Abajo, F. J. G. D. *Nano Lett.* **2011**, *11*, 3370–3377.
- (12) Echtermeyer, T. J.; Britnell, L.; Jasnós, P. K.; Lombardo, A.; Gorbachev, R. V.; Grigorenko, A. N.; Geim, A. K.; Ferrari, A. C.; Novoselov, K. S. *Nature Commun.* **2011**, *2*, 458.
- (13) Liu, Y.; Cheng, R.; Liao, L.; Zhou, H.; Bai, J.; Liu, G.; Liu, L.; Huang, Y.; Duan, X. *Nature Commun.* **2011**, *2*, 579.
- (14) Chen, J.; Badioli, M.; Alonso-González, P.; Thongrattanasiri, S.; Huth, F.; Osmond, J.; Spasenović, M.; Centeno, A.; Pesquera, A.; Godignon, P.; Elorza, A. Z.; Camara, N.; García de Abajo, F. J.; Hillenbrand, R.; Koppens, F. H. L. *Nature* **2012**, *487*, 77–81.
- (15) Fei, Z.; Rodin, A. S.; Andreev, G. O.; Bao, W.; McLeod, A. S.; Wagner, M.; Zhang, L. M.; Zhao, Z.; Thiemens, M.; Dominguez, G.; Fogler, M. M.; Castro Neto, A. H.; Lau, C. N.; Keilmann, F.; Basov, D. N. *Nature* **2012**, *487*, 82–5.
- (16) Jablan, M.; Buljan, H.; Soljačić, M. *Phys. Rev. B* **2009**, *80*, 1–7.
- (17) Gan, X.; Mak, K. F.; Gao, Y.; You, Y.; Hatami, F.; Hone, J.; Heinz, T. F.; Englund, D. *Nano Lett.* **2012**, *12*, 5626–5631.
- (18) Mak, K.; Lui, C.; Shan, J.; Heinz, T. *Phys. Rev. Lett.* **2009**, *102*, 100–103.
- (19) Lu, C.; Fu, Q.; Huang, S.; Liu, J. *Nano Lett.* **2004**, *4*, 623–627.
- (20) Wang, F.; Zhang, Y.; Tian, C.; Girit, C.; Zettl, A.; Crommie, M.; Shen, Y. R. *Science* **2008**, *320*, 206–9.
- (21) Li, Z. Q.; Henriksen, E. A.; Jiang, Z.; Hao, Z.; Martin, M. C.; Kim, P.; Stormer, H. L.; Basov, D. N. *Nature Phys.* **2008**, *4*, 532–535.
- (22) Gao, J.; McMillan, J. F.; Wu, M.-C.; Zheng, J.; Assefa, S.; Wong, C. W. *Appl. Phys. Lett.* **2010**, *96*, 51123.
- (23) Akahane, Y.; Asano, T.; Song, B.-S.; Noda, S. *Nature* **2003**, *425*, 944–947.
- (24) Dean, C. R.; Young, A. F.; Meric, I.; Lee, C.; Wang, L.; Sorgenfrei, S.; Watanabe, K.; Taniguchi, T.; Kim, P.; Shepard, K. L.; Hone, J. *Nature Nanotechnol.* **2010**, *5*, 722–6.
- (25) Englund, D.; Faraon, A.; Fushman, I.; Stoltz, N.; Petroff, P.; Vuckovic, J. *Nature* **2007**, *450*, 857–861.
- (26) Srinivasan, K.; Barclay, P.; Borselli, M.; Painter, O. *Phys. Rev. B* **2004**, *70*, 081306.
- (27) Akahane, Y.; Asano, T.; Song, B.-S.; Noda, S. *Opt. Express* **2005**, *13*, 1202–1214.
- (28) Joannopoulos, J. D.; Johnson, S. G.; Winn, J. N.; Meade, R. D. *Photonic Crystals: Molding the Flow of Light*, 2nd ed.; Princeton University Press: Princeton, NJ, 2008.
- (29) Peres, N. M. R.; Stauber, T.; Castro Neto, A. H. *Europhys. Lett.* **2008**, *84*, 38002.
- (30) Reed, G. T.; Mashanovich, G.; Gardes, F. Y.; Thomson, D. J. *Nat. Photonics* **2010**, *4*, 518–526.
- (31) Carbotte, J. P.; Nicol, E. J.; Sharapov, S. G. *Phys. Rev. B* **2010**, *1*–19.
- (32) Mikhailov, S.; Ziegler, K. *Phys. Rev. Lett.* **2007**, *99*, 1–4.
- (33) Lu, Z.; Zhao, W. J. *Opt. Soc. Am. B* **2012**, *29*, 1490–1496.
- (34) Ozel, T.; Gaur, A.; Rogers, J. A.; Shim, M. *Nano Lett.* **2005**, *5*, 905–911.
- (35) Liu, M.; Yin, X.; Zhang, X. *Nano Lett.* **2012**, *12*, 1482–5.
- (36) Miller, D. A. B. *Proc. IEEE* **2009**, *97*, 1166–1185.

(37) Baehr-jones, T.; Ding, R.; Liu, Y.; Ayazi, A.; Pinguet, T.; Nicholas, C.; Streshinsky, M.; Lee, P.; Zhang, Y.; Lim, A. E.-j.; Teo, S. H.-g.; Lo, G.-q.; Hochberg, M. *Opt. Express* **2012**, *20*, 12014–12020.